Advances in Materials Research, *Vol. 15, No. 1 (2026) 1-21*
https://doi.org/10.12989/amr.2026.15.1.001

Techno-Press

Management of transient dynamic deflection in graphene-reinforced composite structures

Anber Abraheem Shlash Mohammad[1], Suleiman Ibrahim Mohammad*[2,3], Asokan Vasudevan[4,5], Badrea Al Oraini[6], Mohammad Faleh Ahmmad Hunitie[7]

[1]*Digital Marketing Department, Faculty of Administrative and Financial Sciences, University of Petra, Jordan*
[2]*Electronic Marketing and Social Media, Economic and Administrative Sciences, Zarqa University, Jordan*
[3]*Research follower, INTI International University, 71800 Negeri Sembilan, Malaysia*
[4]*Faculty of Business and Communications, INTI International University, 71800 Negeri Sembilan, Malaysia*
[5]*Shinawatra University, 99 Moo 10, Bangtoey, Samkhok, Pathum Thani 12160 Thailand*
[6]*Department of Business Administration, College of Business and Economics, Qassim University, Qassim – Saudi Arabia*
[7]*Department of Public Administration, School of Business, University of Jordan, Jordan*

(Received August 6, 2025, Revised December 23, 2025, Accepted December 31, 2026)

Abstract. The current research examines the transient dynamic deflection response of graphene-reinforced composite structures when subjected to external forces. Analytical solutions are specifically provided for the vibration of a rectangular composite plate that is ultimately loaded and is based on the sinusoidal shear deformation theory (SSDT). The equations of motion are derived from Hamilton's principle, considering shear deformation and bending. A Fourier series expansion is applied to the system response analysis, which allows for the quick calculation of transient deflections by breaking the problem down into harmonic components. One of the major advancements of this study is the application of Laplace transform inversion via the modified Dubner and Abate formulation, which greatly improves both the accuracy and speed of solving transient dynamic problems in composite materials. The investigation of graphene's impact on damping, natural frequencies, and overall dynamic stability of the composite structure is done along with the critical insights into its performance at different excitation frequencies. The findings indicate that the vibrational damping of graphene-based composites is better than that of conventional materials and that they also exhibit different resonance behaviors, which can be advantageous for the East and West coast engineering applications. The analytical framework presented in this paper can predict the dynamic response of graphene-reinforced composite plates and thus help in the design of structural materials that are more robust and resilient under dynamic loading conditions.

Keywords: graphene-reinforced composites; laplace transform inversion; management; sinusoidal shear deformation theory; transient dynamic deflection

1. Introduction

Composite structures have been unprecedentedly pivotal in today's engineering arena due to the fact that they can incorporate the good points of various materials and thus, mechanically they

*Corresponding author, Ph.D., E-mail: dr_sliman@yahoo.com

ISSN: 2234-0912 (Print), 2234-179X (Online)

are great, such as they possess high strength-to-weight ratios and long-lasting [1]. The constant heavy load on light and high-performance materials in industries like aerospace, automotive, and civil engineering etc., has led to the growth of advanced composite materials [2]. Usually, these types of structures comprise two or sometimes more materials which, when united, result in a super-material with unmatched properties compared to those of the individual components [3]. The flexibility of composites' features provides the engineers with a great level of customization to adjust the structure's characteristics to fit the requirements of the moment, such as thermal, electric, and mechanical performance [4]. Moreover, composite materials have been repeatedly reported to have a lot of resistance to corrosion, fatigue, and wear, so they can be used in harsh environmental conditions [5]. The creation of composites with refined properties for particular uses has given birth to potential structural designs that are, by all means, lighter and more durable [6]. The use of composite structures in engineering has also been a big factor contributing to sustainability because it can help to greatly reduce the amount of material consumed and thus the energy used, making the environmental impact lower [7]. The demand for higher efficiency and performance in engineering works is still on the rise, and this has made the role of composite materials in all the processes of design and manufacturing more and more significant [8]. One of the major reasons has been the addition of new graphitic fibers or graphene to the mix, which has taken the material far beyond its limits and provided awesomely super mechanical properties such as elevated strengths, stiffness, and damping [9]. Consequently, there is no other way than to continue the investigations and advancements of composite constructions in the field of engineering design since they make it possible to open up the area of efficient, durable, and lower-cost solutions for different industries [10].

Stability analysis is an essential part of engineering design, as it guarantees the safety and reliability of the structures and systems in all kinds of loading situations [11]. For the engineers, the stability of the materials and the structures is the most important factor in preventing the tragic accidents and providing the long-term use of the structures [12]. The stability of the design to the operational loads, environmental forces, and the dynamic conditions is critical in aerospace, civil, mechanical, and structural engineering for the usability and life of the design [13]. Instabilities can't help but cause deformations, pains, or even total collapse of the structure; hence, stability analysis is necessary throughout the design. Stability analysis is the main tool used by engineers to foresee the behavior of structures under both normal and extreme conditions [14]. Moreover, stability analysis results in good material selection, design changes, and safety measures [15]. The procedure comprises measuring the response of a system to the loads applied, geometry changes, or environmental influences like temperature or pressure variation [16]. Stability analysis is a strategic process in finding the unstable state or the critical load at which a system might fail and the system might fail or enter an unstable state, such as buckling in a column or flutter in a wing [17]. It enables the engineer to build up the design strength while at the same time cutting down on weight, material, and cost [18]. Besides, failure predictions are so accurate that they allow engineers to make structures even more robust; hence the chances of structural failure, costly repairs, downtime, and accidents are reduced [19]. In addition to this, stability analysis is an essential step in the process of dynamic systems optimization, wherein the performance of mechanical parts or equipment relies on their capability to produce stable oscillations or movements [20]. As the engineering industry progresses towards using more sophisticated materials like composites and nanomaterials, stability analysis remains a complex and critical issue [21]. The trend of increasing automation, robotics, and artificial intelligence in engineering systems has also raised the need for stability assessments that are highly sophisticated in order to

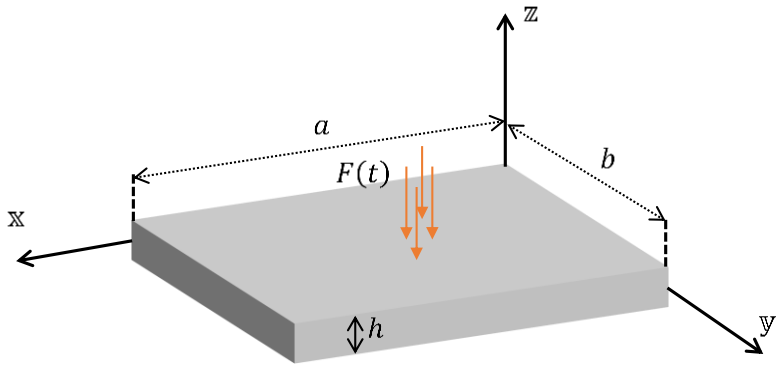

Figure 1. Diagrammatic illustration of a rectangular plate under mechanical stress

avoid failures in the operation [22]. In this situation, stability analysis is a crucial factor in confirming that the systems are capable of not only maintaining but also performing well under changes in load or conditions [23]. Nonetheless, the stability analysis is not just about the safety of the project but also about its economic viability and environmental sustainability in the long run [24]. By adopting a stability-first approach, engineers can contribute to the development of modern infrastructure, transportation, and industrial applications that are not only resilient, efficient but also cost-effective [25].

For the first time, the research investigates the dynamic behavior of composite plates reinforced with graphene when external forces are applied, and the main objective is to manage the transient deflection. The analytical solutions are derived using SSDT for the vibration response of a rectangular composite plate subjected to external dynamic loading. Hamilton's principle is employed to arrive at the governing equations, which include the effects of shear and bending in the composite structure. To find the transient response, a Fourier series expansion is used, which allows the problem to be divided into harmonic components. Furthermore, the time-domain solutions are computed efficiently with the help of the Laplace transform inversion technique based on Dubner and Abate's modified algorithm. The outcomes reveal that the incorporation of graphene influences the structural damping, resonance frequencies, and dynamic stability of the composite plate during the whole cycle of its vibration. The presence of graphene facilitates the dissipation of energy and modifies the vibration traits, thus making the use of materials in vibration-sensitive applications more efficient. The paper contributes significantly by providing a better understanding of the fabricating strategies as well as the material selection of composite materials that would be used in areas where dynamic response is an important factor, especially for structures that are often subjected to periodic or impulsive excitations. The analytical approach is, therefore, a trustworthy means for estimating the transient dynamic behavior of composite plates Strengthened by graphene, rendering it applicable in many areas including aerospace, civil, and mechanical engineering, where it is anticipated that the technology will thrive.

2. Data analysis

This structure's whole geometry is shown in Fig. 1 along with a three-dimensional schematic representation.

2.1 Material properties

Using a modified formulation of the Halpin-Tsai correlation, the following formula was extracted to find the GPLR nanocomposite material's effective elastic modulus [26]:

$$E_c(\mathbb{z}) = -\frac{3}{8}\frac{1+\xi_L\eta_L V_{GPL}}{\eta_L V_{GPL}-1}\times E_m - \frac{5}{8}\frac{1+\xi_W\eta_W V_{GPL}}{\eta_W V_{GPL}-1}\times E_m \tag{1}$$

where $\xi_L = 2\frac{L_{GPL}}{t_{GPL}}$, $\xi_W = 2\frac{W_{GPL}}{t_{GPL}}$, $V^*_{GPL} = \frac{W_{GPL}}{\left(\frac{\rho_{GPL}}{\rho_m}\right)(1-W_{GPL})+W_{GPL}}$, $\eta_W = -\frac{1-\left(\frac{E_{GPL}}{E_m}\right)}{\xi_W+\left(\frac{E_{GPL}}{E_m}\right)}$, and $\eta_L = \frac{\left(\frac{E_{GPL}}{E_m}\right)-1}{\left(\frac{E_{GPL}}{E_m}\right)+\xi_L}$. The law of mixtures would be used to determine the composite plate's effective mass density and Poisson's ratio [27]:

$$\begin{aligned}\rho_c(\mathbb{z}) &= \rho_{GPL}V_{GPL} + \rho_m(1-V_{GPL}),\\ \nu_c(\mathbb{z}) &= \nu_{GPL}V_{GPL} + \nu_m(1-V_{GPL}).\end{aligned} \tag{2}$$

whereas the definition of the effective shear modulus is [28]

$$G_c(\mathbb{z}) = \frac{E_c(\mathbb{z})}{2\left(1+\nu_c(\mathbb{z})\right)} \tag{3}$$

In the thickness direction of the structure, we select three different GPL scattering patterns. The analytical expressions for these patterns are as follows

$$\begin{aligned}&\text{GPL-X: } V_{GPL} = 4V^*_{GPL}\frac{|\mathbb{z}|}{h},\\ &\text{GPL-O: } V_{GPL} = 2V^*_{GPL}\left(1-2\frac{|\mathbb{z}|}{h}\right),\\ &\text{GPL-UD: } V_{GPL} = V^*_{GPL}\end{aligned} \tag{4}$$

where $\mathbb{z} = \frac{(k-1)h}{N_L-1} - \frac{h}{2}$, $k = 1, \ldots, N_L$. Also, the material characteristics are reported in Ref. [29].

2.2 Kinematic relations

The displacement components of the specified improved silicon solar cell can be described as follows using the sinusoidal shear deformation theory (SSDT):

$$\mathbb{u}(\mathbb{x},\mathbb{y},\mathbb{z},t) = \mathbb{u}_0(\mathbb{x},\mathbb{y},t) - \mathbb{z}\frac{\partial \mathbb{w}_0(\mathbb{x},\mathbb{y},t)}{\partial \mathbb{x}} + \frac{h}{\pi}sin\left(\frac{\pi\mathbb{z}}{h}\right)\left(\frac{\partial \mathbb{w}_0(\mathbb{x},\mathbb{y},t)}{\partial \mathbb{x}} - \mathbb{G}_{\mathbb{x}}(\mathbb{x},\mathbb{y},t)\right), \tag{5a}$$

$$\mathbb{v}(\mathbb{x},\mathbb{y},\mathbb{z},t) = \mathbb{v}_0(\mathbb{x},\mathbb{y},t) - \mathbb{z}\frac{\partial \mathbb{w}_0(\mathbb{x},\mathbb{y},t)}{\partial \mathbb{y}} + \frac{h}{\pi}sin\left(\frac{\pi\mathbb{z}}{h}\right)\left(\frac{\partial \mathbb{w}_0(\mathbb{x},\mathbb{y},t)}{\partial \mathbb{y}} - \mathbb{G}_{\mathbb{y}}(\mathbb{x},\mathbb{y},t)\right), \tag{5b}$$

$$\mathbb{w}(\mathbb{x},\mathbb{y},\mathbb{z},t) = \mathbb{w}_0(\mathbb{x},\mathbb{y},t). \tag{5c}$$

where $\mathbb{u}$, $\mathbb{v}$, and $\mathbb{w}$ are the $\mathbb{x}$-, $\mathbb{y}$-, and $\mathbb{z}$-components of the displacement vector, and $\mathbb{G}_{\mathbb{x}}$ and $\mathbb{G}_{\mathbb{y}}$ are the angles of rotation of the cross sections around the $\mathbb{y}$ and $\mathbb{x}$ axes at any point on the microplate's mid-plane, respectively. Furthermore, the microplate's mid-plane displacements in the $\mathbb{x}$-, $\mathbb{y}$-, and $\mathbb{z}$ axes are denoted by $\mathbb{u}_0$, $\mathbb{v}_0$ and $\mathbb{w}_0$. According to the introduced displacement, the strain

components are shown as [30].

$$\mathcal{E}_{\mathbb{x}\mathbb{x}} = \frac{\partial \mathbb{u}}{\partial \mathbb{x}}, \mathcal{E}_{\mathbb{y}\mathbb{y}} = \frac{\partial \mathbb{v}}{\partial \mathbb{y}}, \mathcal{E}_{\mathbb{x}\mathbb{y}} = \frac{1}{2}\frac{\partial \mathbb{v}}{\partial \mathbb{x}} + \frac{1}{2}\frac{\partial \mathbb{u}}{\partial \mathbb{y}}, \mathcal{E}_{\mathbb{x}\mathbb{z}} = \frac{1}{2}\left(\frac{\partial \mathbb{w}}{\partial \mathbb{x}} + \frac{\partial \mathbb{u}}{\partial \mathbb{z}}\right), \mathcal{E}_{\mathbb{y}\mathbb{z}} = \frac{1}{2}\left(\frac{\partial \mathbb{w}}{\partial \mathbb{y}} + \frac{\partial \mathbb{v}}{\partial \mathbb{z}}\right). \tag{6}$$

The constitutive relations [30] of the silicon solar cell is

$$\begin{Bmatrix} \mathfrak{T}_{\mathbb{x}\mathbb{x}} \\ \mathfrak{T}_{\mathbb{y}\mathbb{y}} \\ \mathfrak{T}_{\mathbb{y}\mathbb{z}} \\ \mathfrak{T}_{\mathbb{x}\mathbb{z}} \\ \mathfrak{T}_{\mathbb{x}\mathbb{y}} \end{Bmatrix} = \begin{Bmatrix} \mathfrak{x}_{11} & \mathfrak{x}_{12} & 0 & 0 & 0 \\ \mathfrak{x}_{21} & \mathfrak{x}_{22} & 0 & 0 & 0 \\ 0 & 0 & \mathfrak{x}_{44} & 0 & 0 \\ 0 & 0 & 0 & \mathfrak{x}_{55} & 0 \\ 0 & 0 & 0 & 0 & \mathfrak{x}_{66} \end{Bmatrix} \begin{Bmatrix} \mathcal{E}_{\mathbb{x}\mathbb{x}} \\ \mathcal{E}_{\mathbb{y}\mathbb{y}} \\ 2\mathcal{E}_{\mathbb{y}\mathbb{z}} \\ 2\mathcal{E}_{\mathbb{x}\mathbb{z}} \\ 2\mathcal{E}_{\mathbb{x}\mathbb{y}} \end{Bmatrix} \tag{7}$$

where the shear stress factors are $\mathfrak{T}_{\mathbb{y}\mathbb{z}}$, $\mathfrak{T}_{\mathbb{x}\mathbb{z}}$ and $\mathfrak{T}_{\mathbb{x}\mathbb{y}}$, while the normal stress factors are $\mathfrak{T}_{\mathbb{x}\mathbb{x}}$ and $\mathfrak{T}_{\mathbb{y}\mathbb{y}}$. The silicon solar cell's stiffness coefficient is represented by $\mathfrak{x}_{ij}$, and there are

$$\mathfrak{x}_{11} = \frac{E_c}{1-\nu_c^2}, \mathfrak{x}_{12} = \mathfrak{x}_{21} = \frac{\nu_c E_c}{1-\nu_c^2}, \mathfrak{x}_{22} = \frac{E_c}{1-\nu_c^2}, \tag{8a}$$

$$\mathfrak{x}_{66} = \frac{E_c}{2(1+\nu_c)}, \mathfrak{x}_{44} = \frac{E_c}{2(1+\nu_c)}, \mathfrak{x}_{55} = \frac{E_c}{2(1+\nu_c)}. \tag{8b}$$

3. Governing equations

The plate's strain energy is defined as follows:

$$U = \int_V \left(\mathfrak{T}_{\mathbb{x}\mathbb{x}}\mathcal{E}_{\mathbb{x}\mathbb{x}} + \mathfrak{T}_{\mathbb{y}\mathbb{y}}\mathcal{E}_{\mathbb{y}\mathbb{y}} + 2\mathfrak{T}_{\mathbb{x}\mathbb{z}}\mathcal{E}_{\mathbb{x}\mathbb{z}} + 2\mathfrak{T}_{\mathbb{x}\mathbb{y}}\mathcal{E}_{\mathbb{x}\mathbb{y}} + 2\mathfrak{T}_{\mathbb{y}\mathbb{z}}\mathcal{E}_{\mathbb{y}\mathbb{z}}\right)dV \tag{9}$$

where A is area of the plate. By operating $d\mathbb{z}$ on $\mathfrak{T}_{ij}$ the resultant components are defined as:

$$\left\{\mathfrak{A}_{ij}, \mathfrak{B}_{ij}, \mathfrak{C}_{ij}, \mathfrak{C}^*_{ij}, \mathfrak{D}_{ij}\right\} = \int_{-\frac{h}{2}}^{\frac{h}{2}} \left(1, \mathbb{z}, \frac{h}{\pi} sin\left(\frac{\pi \mathbb{z}}{h}\right), \frac{\pi}{h} sin\left(\frac{\pi \mathbb{z}}{h}\right), cos\left(\frac{\pi \mathbb{z}}{h}\right)\right) \mathfrak{T}_{ij} d\mathbb{z}, \tag{10}$$

The strain energy has the following final variation form upon substitution of the consequent components from Eqs. (9), (10):

$$\begin{aligned} \delta U = \iint \Bigg\{ \Bigg(\left(-\frac{\partial \mathfrak{A}_{\mathbb{x}\mathbb{x}}}{\partial \mathbb{x}} - \frac{\partial \mathfrak{A}_{\mathbb{x}\mathbb{y}}}{\partial \mathbb{y}}\right)\delta \mathbb{u} + \left(-\frac{\partial \mathfrak{A}_{\mathbb{x}\mathbb{y}}}{\partial \mathbb{x}} - \frac{\partial \mathfrak{A}_{\mathbb{y}\mathbb{y}}}{\partial \mathbb{y}}\right)\delta \mathbb{v} + \left(-\frac{\partial^2 \mathfrak{B}_{\mathbb{x}\mathbb{x}}}{\partial \mathbb{x}^2} + \frac{\partial^2 \mathfrak{C}_{\mathbb{x}\mathbb{x}}}{\partial \mathbb{x}^2} - 2\frac{\partial^2 \mathfrak{B}_{\mathbb{x}\mathbb{y}}}{\partial \mathbb{y}\partial \mathbb{x}} + \\ 2\frac{\partial^2 \mathfrak{C}_{\mathbb{x}\mathbb{y}}}{\partial \mathbb{y}\partial \mathbb{x}} - \frac{\partial \mathfrak{D}_{\mathbb{x}\mathbb{z}}}{\partial \mathbb{x}} - \frac{\partial^2 \mathfrak{B}_{\mathbb{y}\mathbb{y}}}{\partial \mathbb{y}^2} + \frac{\partial^2 \mathfrak{C}_{\mathbb{y}\mathbb{y}}}{\partial \mathbb{y}^2} - \frac{\partial \mathfrak{D}_{\mathbb{y}\mathbb{z}}}{\partial \mathbb{y}}\right)\delta \mathbb{w} + \left(\frac{\partial \mathfrak{C}_{\mathbb{x}\mathbb{x}}}{\partial \mathbb{x}} + \frac{\partial \mathfrak{C}_{\mathbb{x}\mathbb{y}}}{\partial \mathbb{y}} - \mathfrak{D}_{\mathbb{x}\mathbb{z}}\right)\delta \mathbb{G}_{\mathbb{x}} + \left(\frac{\partial \mathfrak{C}_{\mathbb{x}\mathbb{y}}}{\partial \mathbb{x}} + \frac{\partial \mathfrak{C}_{\mathbb{y}\mathbb{y}}}{\partial \mathbb{y}} - \right. \\ \left. \mathfrak{D}_{\mathbb{y}\mathbb{z}}\right)\delta \mathbb{G}_{\mathbb{y}} \Bigg) \Bigg\} dA \end{aligned} \tag{11}$$

where U_1 and U_2 represent the classical and non-classical components of the strain energy, respectively. The variability in kinetic energy is expressed as follows:

$$\delta T = \iint \left\{ \left(-\mathbb{T}_0 \frac{\partial^2 \mathbb{u}}{\partial t^2} + \mathbb{T}_1 \frac{\partial^3 \mathbb{w}}{\partial \mathbb{x}\partial t^2} - \mathbb{T}_3 \frac{\partial^3 \mathbb{w}}{\partial \mathbb{x}\partial t^2} + \mathbb{T}_3 \frac{\partial^2 \mathbb{G}_{\mathbb{x}}}{\partial t^2}\right)\delta \mathbb{u} + \left(-\mathbb{T}_0 \frac{\partial^2 \mathbb{v}}{\partial t^2} + \mathbb{T}_1 \frac{\partial^3 \mathbb{w}}{\partial \mathbb{y}\partial t^2} - \right. \right. \tag{12}$$

$$\mathbb{T}_3\frac{\partial^3 \mathbb{w}}{\partial \mathbb{y}\partial t^2}+\mathbb{T}_3\frac{\partial^2}{\partial t^2}\mathbb{G}_{\mathbb{y}}\Big)\delta \mathbb{v}+\Big(-\mathbb{T}_1\frac{\partial^3 \mathbb{u}}{\partial \mathbb{x}\partial t^2}+\mathbb{T}_3\frac{\partial^3 \mathbb{u}}{\partial \mathbb{x}\partial t^2}+\mathbb{T}_2\frac{\partial^4 \mathbb{w}}{\partial \mathbb{x}^2\partial t^2}-2\mathbb{T}_5\frac{\partial^4 \mathbb{w}}{\partial \mathbb{x}^2\partial t^2}+\mathbb{T}_5\frac{\partial^3 \mathbb{G}_{\mathbb{x}}}{\partial \mathbb{x}\partial t^2}+$$
$$\mathbb{T}_4\frac{\partial^4 \mathbb{w}}{\partial \mathbb{x}^2\partial t^2}-\mathbb{T}_4\frac{\partial^3 \mathbb{G}_{\mathbb{x}}}{\partial \mathbb{x}\partial t^2}-\mathbb{T}_1\frac{\partial^3 \mathbb{v}}{\partial \mathbb{y}\partial t^2}+\mathbb{T}_3\frac{\partial^3 \mathbb{v}}{\partial \mathbb{y}\partial t^2}+\mathbb{T}_2\frac{\partial^4 \mathbb{w}}{\partial \mathbb{y}^2\partial t^2}-2\mathbb{T}_5\frac{\partial^4 \mathbb{w}}{\partial \mathbb{y}^2\partial t^2}+\mathbb{T}_5\frac{\partial^3 \mathbb{G}_{\mathbb{y}}}{\partial \mathbb{y}\partial t^2}+$$
$$\mathbb{T}_4\frac{\partial^4 \mathbb{w}}{\partial \mathbb{y}^2\partial t^2}-\mathbb{T}_4\frac{\partial^3 \mathbb{G}_{\mathbb{y}}}{\partial \mathbb{y}\partial t^2}-\mathbb{T}_0\frac{\partial^2 \mathbb{w}}{\partial t^2}\Big)\delta \mathbb{w}+\Big(\mathbb{T}_3\frac{\partial^2 \mathbb{u}}{\partial t^2}-\mathbb{T}_5\frac{\partial^3 \mathbb{w}}{\partial \mathbb{x}\partial t^2}+\mathbb{T}_4\frac{\partial^3 \mathbb{w}}{\partial \mathbb{x}\partial t^2}-\mathbb{T}_4\frac{\partial^2 \mathbb{G}_{\mathbb{x}}}{\partial t^2}\Big)\delta \mathbb{G}_{\mathbb{x}}+$$
$$\Big(\mathbb{T}_3\frac{\partial^2 \mathbb{v}}{\partial t^2}-\mathbb{T}_5\frac{\partial^3 \mathbb{w}}{\partial \mathbb{y}\partial t^2}+\mathbb{T}_4\frac{\partial^3 \mathbb{w}}{\partial \mathbb{y}\partial t^2}-\mathbb{T}_4\frac{\partial^2 \mathbb{G}_{\mathbb{y}}}{\partial t^2}\Big)\delta \mathbb{G}_{\mathbb{y}}\Big\}dA$$

where the integration constants are defined as:

$$\{\mathbb{T}_0,\mathbb{T}_1,\mathbb{T}_2,\mathbb{T}_3,\mathbb{T}_4,\mathbb{T}_5\}=\int_{-\frac{h}{2}}^{\frac{h}{2}}\rho_c\left\{1,\mathbb{z},\mathbb{z}^2,\frac{h}{\pi}sin(\frac{\pi\mathbb{z}}{h}),\frac{h^2}{\pi^2}sin2(\frac{\pi\mathbb{z}}{h}),\frac{h\mathbb{z}}{\pi}sin(\frac{\pi\mathbb{z}}{h})\right\}d\mathbb{z} \tag{13}$$

Also, the virtual work done by external forces δW of the system can be expressed respectively as

$$\delta W=\iint F\delta \mathbb{w}dA \tag{14}$$

In which, $F=Psin(\Omega_{ext}t)$ where P is the load intensity and Ω_{ext} denotes the excitation frequency. In addition, the dissipation energy by damper can be written as:

$$\delta D=\iint C_d\frac{\partial \mathbb{w}}{\partial t}\frac{\partial \delta \mathbb{w}}{\partial t}dA \tag{15}$$

where C_d is the damping coefficient of the viscoelastic medium.

Five equations of motion that control the issue are derived using Hamilton's principle as follows:

$$-\mathbb{T}_0\frac{\partial^2 \mathbb{u}}{\partial t^2}+\mathbb{T}_1\frac{\partial^3 \mathbb{w}}{\partial \mathbb{x}\partial t^2}-\mathbb{T}_3\frac{\partial^3 \mathbb{w}}{\partial \mathbb{x}\partial t^2}+\mathbb{T}_3\frac{\partial^2 \mathbb{G}_{\mathbb{x}}}{\partial t^2}+\frac{\partial \mathfrak{U}_{\mathbb{xx}}}{\partial \mathbb{x}}+\frac{\partial \mathfrak{U}_{\mathbb{xy}}}{\partial \mathbb{y}}=0, \tag{16a}$$

$$\mathbb{T}_3\frac{\partial^2 \mathbb{G}_{\mathbb{y}}}{\partial t^2}+\mathbb{T}_1\frac{\partial^3 \mathbb{w}}{\partial \mathbb{y}\partial t^2}-\mathbb{T}_0\frac{\partial^2 \mathbb{v}}{\partial t^2}-\mathbb{T}_3\frac{\partial^3 \mathbb{w}}{\partial \mathbb{y}\partial t^2}+\frac{\partial \mathfrak{U}_{\mathbb{xy}}}{\partial \mathbb{x}}+\frac{\partial \mathfrak{U}_{\mathbb{yy}}}{\partial \mathbb{y}}=0, \tag{16b}$$

$$\begin{aligned}&\mathbb{T}_3\frac{\partial^3 \mathbb{u}}{\partial \mathbb{x}\partial t^2}-\mathbb{T}_1\frac{\partial^3 \mathbb{u}}{\partial \mathbb{x}\partial t^2}+\mathbb{T}_3\frac{\partial^3 \mathbb{v}}{\partial \mathbb{y}\partial t^2}-\mathbb{T}_1\frac{\partial^3 \mathbb{v}}{\partial \mathbb{y}\partial t^2}-2\mathbb{T}_5\frac{\partial^4 \mathbb{w}}{\partial \mathbb{x}^2\partial t^2}-\mathbb{T}_0\frac{\partial^2 \mathbb{w}}{\partial t^2}+\mathbb{T}_4\frac{\partial^4 \mathbb{w}}{\partial \mathbb{y}^2\partial t^2}+\mathbb{T}_2\frac{\partial^4 \mathbb{w}}{\partial \mathbb{y}^2\partial t^2}-\\&2\mathbb{T}_5\frac{\partial^4 \mathbb{w}}{\partial \mathbb{y}^2\partial t^2}+\mathbb{T}_2\frac{\partial^4 \mathbb{w}}{\partial \mathbb{x}^2\partial t^2}+\mathbb{T}_4\frac{\partial^4 \mathbb{w}}{\partial \mathbb{x}^2\partial t^2}-\frac{\partial^2 \mathfrak{C}_{\mathbb{xx}}}{\partial \mathbb{x}^2}-\frac{2\partial^2 \mathfrak{C}_{\mathbb{xy}}}{\partial \mathbb{y}\partial \mathbb{x}}-\frac{\partial^2 \mathfrak{C}_{\mathbb{yy}}}{\partial \mathbb{y}^2}+\mathbb{T}_5\frac{\partial^3 \mathbb{G}_{\mathbb{y}}}{\partial \mathbb{y}\partial t^2}-\mathbb{T}_4\frac{\partial^3 \mathbb{G}_{\mathbb{y}}}{\partial \mathbb{y}\partial t^2}-\\&\mathbb{T}_4\frac{\partial^3 \mathbb{G}_{\mathbb{x}}}{\partial \mathbb{x}\partial t^2}+\mathbb{T}_5\frac{\partial^3 \mathbb{G}_{\mathbb{x}}}{\partial \mathbb{x}\partial t^2}+\frac{\partial^2 \mathfrak{B}_{\mathbb{yy}}}{\partial \mathbb{y}^2}+\frac{2\partial^2 \mathfrak{B}_{\mathbb{xy}}}{\partial \mathbb{y}\partial \mathbb{x}}+\frac{\partial^2 \mathfrak{B}_{\mathbb{xx}}}{\partial \mathbb{x}^2}+\frac{\partial \mathfrak{D}_{\mathbb{yz}}}{\partial \mathbb{y}}+\frac{\partial \mathfrak{D}_{\mathbb{xz}}}{\partial \mathbb{x}}-C_d\frac{\partial \mathbb{w}}{\partial t}+F=0,\end{aligned} \tag{16c}$$

$$\mathbb{T}_3\frac{\partial^2 \mathbb{u}}{\partial t^2}-\mathbb{T}_5\frac{\partial^3 \mathbb{w}}{\partial \mathbb{x}\partial t^2}-\mathbb{T}_4\frac{\partial^2 \mathbb{G}_{\mathbb{x}}}{\partial t^2}+\mathbb{T}_4\frac{\partial^3 \mathbb{w}}{\partial \mathbb{x}\partial t^2}-\frac{\partial \mathfrak{C}_{\mathbb{xx}}}{\partial \mathbb{x}}-\frac{\partial \mathfrak{C}_{\mathbb{xy}}}{\partial \mathbb{y}}+\mathfrak{D}_{\mathbb{xz}}=0, \tag{16d}$$

$$-\mathbb{T}_4\frac{\partial^2 \mathbb{G}_{\mathbb{y}}}{\partial t^2}+\mathbb{T}_3\frac{\partial^2 \mathbb{v}}{\partial t^2}+\mathbb{T}_4\frac{\partial^3 \mathbb{w}}{\partial \mathbb{y}\partial t^2}-\mathbb{T}_5\frac{\partial^3 \mathbb{w}}{\partial \mathbb{y}\partial t^2}-\frac{\partial \mathfrak{C}_{\mathbb{xy}}}{\partial \mathbb{x}}-\frac{\partial \mathfrak{C}_{\mathbb{yy}}}{\partial \mathbb{y}}+\mathfrak{D}_{\mathbb{yz}}=0, \tag{16e}$$

4. Solution method

The subsequent it is possible to employ Fourier expansion, which perfectly satisfies the governing equations and simple boundary conditions.

$$\mathbb{u}_0(\mathbb{x},\mathbb{y},t)=\sum_{m=1}^{\infty}\sum_{n=1}^{\infty}u_{mn}(t)\cos(\alpha_m\mathbb{x})\sin(\beta_n\mathbb{y}) \tag{17a}$$

$$\mathbb{v}_0(\mathbb{x},\mathbb{y},t)=\sum_{m=1}^{\infty}\sum_{n=1}^{\infty}v_{mn}(t)\sin(\alpha_m\mathbb{x})\cos(\beta_n\mathbb{y}) \tag{17b}$$

$$\mathbb{w}_0(\mathbb{x},\mathbb{y},t)=\sum_{m=1}^{\infty}\sum_{n=1}^{\infty}w_{mn}(t)\sin(\alpha_m\mathbb{x})\sin(\beta_n\mathbb{y}) \tag{17c}$$

$$\mathbb{G}_{\mathbb{x}}(\mathbb{x},\mathbb{y},t)=\sum_{m=1}^{\infty}\sum_{n=1}^{\infty}x_{mn}(t)\cos(\alpha_m\mathbb{x})\sin(\beta_n\mathbb{y}) \tag{17d}$$

$$\mathbb{G}_{\mathbb{y}}(\mathbb{x},\mathbb{y},t)=\sum_{m=1}^{\infty}\sum_{n=1}^{\infty}y_{mn}(t)\sin(\alpha_m\mathbb{x})\cos(\beta_n\mathbb{y}) \tag{17e}$$

where in Eqs. (17a-e), $\alpha_m=m\pi/a$ and $\beta_n=n\pi/b$. Also m and n are the number of half waves through the length and width of the plate. Therefore, we obtain the following equation by replacing Eqs. (16a-e) with Eqs. (17a-e):

$$\begin{bmatrix}[\mathbb{M}_{11}] & [\mathbb{M}_{12}] & [\mathbb{M}_{13}] & [\mathbb{M}_{14}] & [\mathbb{M}_{15}]\\ [\mathbb{M}_{21}] & [\mathbb{M}_{22}] & [\mathbb{M}_{23}] & [\mathbb{M}_{24}] & [\mathbb{M}_{25}]\\ [\mathbb{M}_{31}] & [\mathbb{M}_{32}] & [\mathbb{M}_{33}] & [\mathbb{M}_{34}] & [\mathbb{M}_{35}]\\ [\mathbb{M}_{41}] & [\mathbb{M}_{42}] & [\mathbb{M}_{43}] & [\mathbb{M}_{44}] & [\mathbb{M}_{45}]\\ [\mathbb{M}_{51}] & [\mathbb{M}_{52}] & [\mathbb{M}_{53}] & [\mathbb{M}_{54}] & [\mathbb{M}_{55}]\end{bmatrix}\begin{Bmatrix}\ddot{u}\\ \ddot{v}\\ \ddot{w}\\ \ddot{x}\\ \ddot{y}\end{Bmatrix}+$$
$$+\begin{bmatrix}[\mathbb{C}_{11}] & [\mathbb{C}_{12}] & [\mathbb{C}_{13}] & [\mathbb{C}_{14}] & [\mathbb{C}_{15}]\\ [\mathbb{C}_{21}] & [\mathbb{C}_{22}] & [\mathbb{C}_{23}] & [\mathbb{C}_{24}] & [\mathbb{C}_{25}]\\ [\mathbb{C}_{31}] & [\mathbb{C}_{32}] & [\mathbb{C}_{33}] & [\mathbb{C}_{34}] & [\mathbb{C}_{35}]\\ [\mathbb{C}_{41}] & [\mathbb{C}_{42}] & [\mathbb{C}_{43}] & [\mathbb{C}_{44}] & [\mathbb{C}_{45}]\\ [\mathbb{C}_{51}] & [\mathbb{C}_{52}] & [\mathbb{C}_{53}] & [\mathbb{C}_{54}] & [\mathbb{C}_{55}]\end{bmatrix}\begin{Bmatrix}\dot{u}\\ \dot{v}\\ \dot{w}\\ \dot{x}\\ \dot{y}\end{Bmatrix}+ \tag{18}$$
$$\begin{bmatrix}[\mathbb{K}_{11}] & [\mathbb{K}_{12}] & [\mathbb{K}_{13}] & [\mathbb{K}_{14}] & [\mathbb{K}_{15}]\\ [\mathbb{K}_{21}] & [\mathbb{K}_{22}] & [\mathbb{K}_{23}] & [\mathbb{K}_{24}] & [\mathbb{K}_{25}]\\ [\mathbb{K}_{31}] & [\mathbb{K}_{32}] & [\mathbb{K}_{33}] & [\mathbb{K}_{34}] & [\mathbb{K}_{35}]\\ [\mathbb{K}_{41}] & [\mathbb{K}_{42}] & [\mathbb{K}_{43}] & [\mathbb{K}_{44}] & [\mathbb{K}_{45}]\\ [\mathbb{K}_{51}] & [\mathbb{K}_{52}] & [\mathbb{K}_{53}] & [\mathbb{K}_{54}] & [\mathbb{K}_{55}]\end{bmatrix}\begin{Bmatrix}u\\ v\\ w\\ x\\ y\end{Bmatrix}=\begin{Bmatrix}\{0\}\\ \{0\}\\ \{F(t)\}\\ \{0\}\\ \{0\}\end{Bmatrix},$$

The following relations result from applying the Laplace transform [31] to Eq. (18) for different boundary conditions.

$$\begin{bmatrix}[\mathbb{M}_{11}] & [\mathbb{M}_{12}] & [\mathbb{M}_{13}] & [\mathbb{M}_{14}] & [\mathbb{M}_{15}]\\ [\mathbb{M}_{21}] & [\mathbb{M}_{22}] & [\mathbb{M}_{23}] & [\mathbb{M}_{24}] & [\mathbb{M}_{25}]\\ [\mathbb{M}_{31}] & [\mathbb{M}_{32}] & [\mathbb{M}_{33}] & [\mathbb{M}_{34}] & [\mathbb{M}_{35}]\\ [\mathbb{M}_{41}] & [\mathbb{M}_{42}] & [\mathbb{M}_{43}] & [\mathbb{M}_{44}] & [\mathbb{M}_{45}]\\ [\mathbb{M}_{51}] & [\mathbb{M}_{52}] & [\mathbb{M}_{53}] & [\mathbb{M}_{54}] & [\mathbb{M}_{55}]\end{bmatrix}\begin{Bmatrix}\mathbb{s}^2\times\hat{u}\\ \mathbb{s}^2\times\hat{v}\\ \mathbb{s}^2\times\hat{w}\\ \mathbb{s}^2\times\hat{x}\\ \mathbb{s}^2\times\hat{y}\end{Bmatrix}+ \tag{19}$$

$$+\begin{bmatrix}[\mathbb{C}_{11}] & [\mathbb{C}_{12}] & [\mathbb{C}_{13}] & [\mathbb{C}_{14}] & [\mathbb{C}_{15}]\\ [\mathbb{C}_{21}] & [\mathbb{C}_{22}] & [\mathbb{C}_{23}] & [\mathbb{C}_{24}] & [\mathbb{C}_{25}]\\ [\mathbb{C}_{31}] & [\mathbb{C}_{32}] & [\mathbb{C}_{33}] & [\mathbb{C}_{34}] & [\mathbb{C}_{35}]\\ [\mathbb{C}_{41}] & [\mathbb{C}_{42}] & [\mathbb{C}_{43}] & [\mathbb{C}_{44}] & [\mathbb{C}_{45}]\\ [\mathbb{C}_{51}] & [\mathbb{C}_{52}] & [\mathbb{C}_{53}] & [\mathbb{C}_{54}] & [\mathbb{C}_{55}]\end{bmatrix}\begin{Bmatrix}\mathbb{s}\times\hat{u}\\ \mathbb{s}\times\hat{v}\\ \mathbb{s}\times\hat{w}\\ \mathbb{s}\times\hat{x}\\ \mathbb{s}\times\hat{y}\end{Bmatrix}+$$

$$\begin{bmatrix}[\mathbb{K}_{11}] & [\mathbb{K}_{12}] & [\mathbb{K}_{13}] & [\mathbb{K}_{14}] & [\mathbb{K}_{15}]\\ [\mathbb{K}_{21}] & [\mathbb{K}_{22}] & [\mathbb{K}_{23}] & [\mathbb{K}_{24}] & [\mathbb{K}_{25}]\\ [\mathbb{K}_{31}] & [\mathbb{K}_{32}] & [\mathbb{K}_{33}] & [\mathbb{K}_{34}] & [\mathbb{K}_{35}]\\ [\mathbb{K}_{41}] & [\mathbb{K}_{42}] & [\mathbb{K}_{43}] & [\mathbb{K}_{44}] & [\mathbb{K}_{45}]\\ [\mathbb{K}_{51}] & [\mathbb{K}_{52}] & [\mathbb{K}_{53}] & [\mathbb{K}_{54}] & [\mathbb{K}_{55}]\end{bmatrix}\begin{Bmatrix}\hat{u}\\ \hat{v}\\ \hat{w}\\ \hat{x}\\ \hat{y}\end{Bmatrix}=\begin{Bmatrix}\{0\}\\ \{0\}\\ \{\hat{F}(\mathbb{s})\}\\ \{0\}\\ \{0\}\end{Bmatrix},$$

Eqs. (5a-c) and (7) will provide the displacements and tension across the plate in a transverse configuration; the displacements and stresses are determined over time by using the Laplace transform inversion on Dubner and Abate's modified formulation [32]; thus, Eq. (20) is the mathematical formula used to carry out the inverse Laplace transform in this research. The displacement for each layer may be obtained by solving Eq. (19) using the layer-wise technique and the Laplace transform [31].

$$\mathbb{f}(t)=\frac{2e^{at}}{T}\left[-\frac{A_0}{2}+\sum_{k=0}^{\infty}\left(A_k cos\left(\frac{2k\pi t}{T}\right)-\mathbb{b}_k sin\left(\frac{2k\pi t}{T}\right)\right)\right] \tag{20}$$

Here

$$A_0=Re[F(a)],\ A_k=Re\left[F\left(a+i\frac{2k\pi}{T}\right)\right],\ \mathbb{b}_k=im\left[F\left(a+i\frac{2k\pi}{T}\right)\right],\\ \mathbb{s}=a+i\frac{2k\pi}{T},\ aT=5. \tag{21}$$

Also, dimensionless quantities are defined by

$$(\bar{u}\quad \bar{v}\quad \bar{w})=\frac{E_M h^3}{P_0 a^4}(u\quad v\quad w),\ \bar{z}=\frac{\mathbb{z}}{h},\ \zeta=\frac{C_d}{C_{cr}},\\ \bar{P}=\frac{P}{P_0},\ P_0=1000\ [\text{KPa}]. \tag{22}$$

5. Results and discussion

5.1 Verification study

In Table 1, the accuracy of the analytical model for static bending of the present study is verified by means of a comparison of its dimensionless center deflection predictions with three established references (Ref. [33-35]). The comparison relates to the case of a square functionally graded (FG) plate subjected to constant load, and the FG power index is the most important parameter determining how the material property varies through the thickness. The results indicate that the current method is in excellent agreement with the referenced solutions at all n_z values. The present model's computed deflections are always compactly located within the very small range of results that have been reported in the literature. For example, at n_z=1, the present result (0.2712) is very close to the cited range between 0.2522 and 0.2905. This close correlation is a strong

Table 1. Comparing the dimensionless center deflections of a square functionally graded plate under a constant load

	n_z			
Method	0	0.5	1	2
Present	0.1714	0.2314	0.2712	0.3117
Ref. [34]	0.1703	0.2232	0.2522	0.2827
Ref. [35]	0.1671	0.2505	0.2905	0.3280
Ref. [33]	0.1722	0.2403	0.2811	0.3221

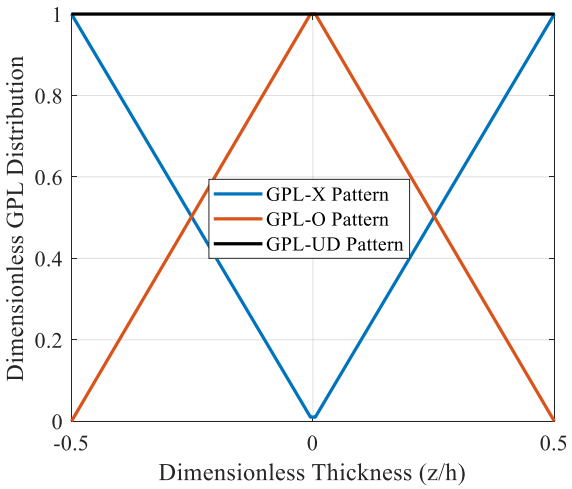

Figure 2. The through-thickness distribution profiles of GPLs in the composite plate

validation for the derivation of equations of motion, for the use of the SSDT kinematics, and for the static case solution methodology. Moreover, the table gives the structural effect of the gradation index: the normalized center deflection increases continuously when n_z is changed from 0 (fully ceramic) to 2. This is mirroring the decline in total bending stiffness that is caused by the change in material composition. The success of the static validation gives room for the confidence of the model's capability of being extended to the more complex analyses of the transient dynamic of graphene-reinforced composites, which are then to be presented as the main content of the paper.

5.2 Parametric results

The through-thickness distribution profiles of GPLs in the composite plate are depicted in Fig. 2, which is a significant design parameter in the analytical model used for the study. The vertical axis (Dimensionless GPL Distribution) indicates the relative concentration of the GPLs, while the horizontal axis covers the distance from the bottom to the top surface of the plate (0.5). Different reinforcement patterns are distinguished and compared: 1. GPL-X Pattern: The GPLs' highest concentration is at the top and bottom surfaces, while the lowest is at the mid-plane. By placing the stiffest material at the farthest point from the neutral axis, this symmetrical, functionally

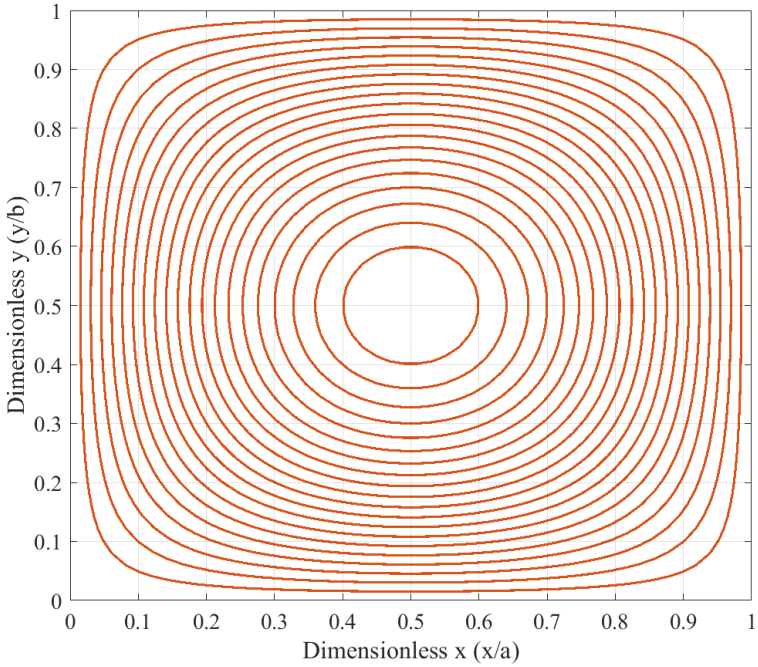

Figure 3. The vibrational response of the rectangular composite plate from a top-down view, as aligned with a planar view

graded distribution maximizes bending stiffness. 2. GPL-O Pattern: The same pattern as the X-pattern but upside-down, where the GPL concentration is the greatest at the mid-plane and the lowest at the surfaces. This arrangement alternates the effects on shear deformation and internal damping characteristics. 3. GPL-UD Pattern: Here, the GPLs are Dispersed Consistently Throughout the entire thickness, hence no variation in concentration. Distributions of this kind directly control the effective material properties (such as elastic modulus and density) at different points through the thickness, which are very important inputs for the SSDT-based equations of motion. The analysis of these different patterns will help to estimate how the spatial arrangement of graphene reinforcement, beyond merely its volume fraction, influences the transient dynamic deflection, natural frequencies, and damping performance predicted by the analytical solution.

Fig. 3 shows the vibrational response of the rectangular composite plate from a top-down view, as aligned with a planar view. The graphs represent the dimensionless planar coordinates, with x/a and y/b scaling from 0 to 1, indicating the plate's length and width, respectively. As the research is devoted to the deflection under external excitation, this image probably shows one of the two main analytical results: 1. The normalized mode shape corresponding to a certain natural frequency, which displays the typical stationary pattern of peaks (anti-nodes) and nodal lines (zero displacement lines) during free vibration. The contour lines or color gradient would represent the relative amplitude of out-of-plane deflection across the plate surface. 2. A snapshot of the transient displacement field at one specific time point after the external force has been applied. This would reveal the deformed shape resulting from the superposition of several excited modes as calculated by the Fourier series expansion and Laplace transform inversion method mentioned in the abstract. The deflection magnitude was most probably visualized by the plot in either a contour map or 3D

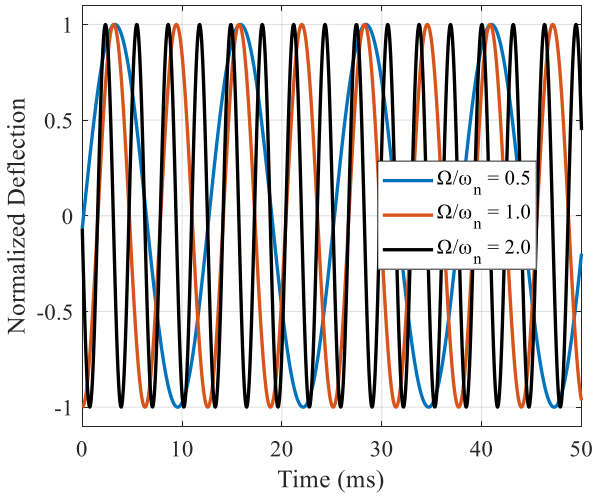

Figure 4. The time history of the plate's normalized central deflection under external harmonic excitation

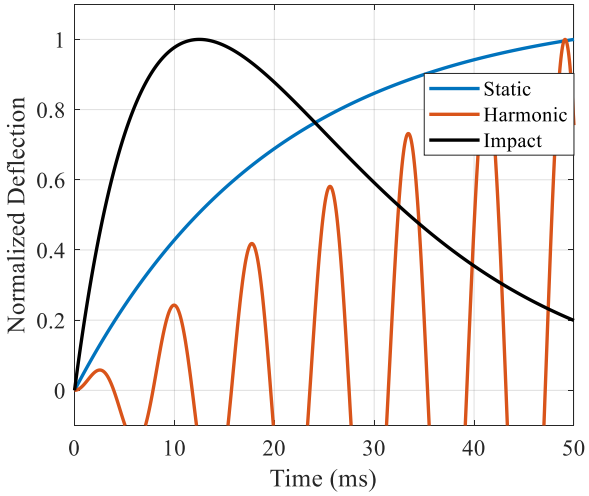

Figure 5. The transient central deflection response of the graphene-reinforced composite plate with the same normalized scale

surface projection. The careful analysis of such a figure makes it possible to confirm the correctness of the analytical solution's boundary conditions and supply critical insights into the nature of the graphene reinforcement patterns' (GPL-X, O, UD) impact not only on the magnitude of dynamic deformation but also on its spatial distribution. Thus, this connects the through-thickness material design (previous figure) directly to the global structural performance.

The time history of the plate's normalized central deflection under external harmonic excitation is illustrated in Fig. 4, indicating the main quasi-static response investigated in this research. The horizontal axis represents time in milliseconds, while the vertical axis signifies normalized deflection, probably with respect to a static reference point. The three curves depicted are for circumstances with varied ratios of excitation frequency to natural frequency (Ω/ω_2), where Ω is

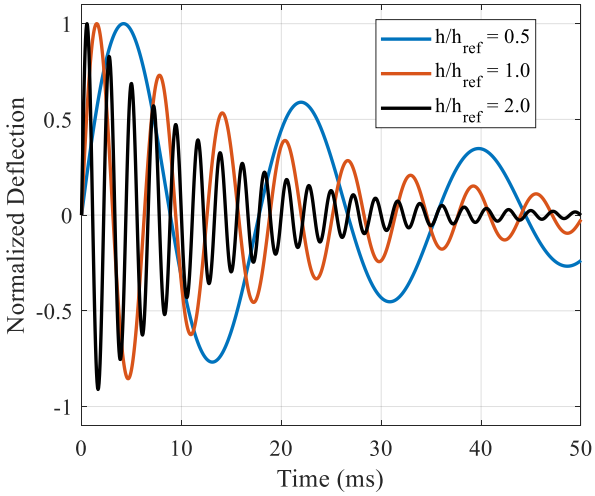

Figure 6. The impact of thickness on the plate's dynamic response, which is an important consideration for structural design

the forcing frequency and ω_n is a pure natural frequency. At $\Omega/\omega_n = 0.5$ (sub-resonance), the response reveals forced oscillations of moderate amplitude. The curve for $\Omega/\omega_n = 1.0$ (resonance) shows the typical large-amplitude oscillatory response, while its decay represents the system's damping capacity. The case of $\Omega/\omega_n = 2.0$ (super-resonance) has the least amplitude, but higher frequency oscillations. These analytical transients are, in fact, the direct products of the Laplace transform inversion technique that is mentioned in the abstract, providing a fast and precise solution. The decay envelope obtained in all cases quantitatively reflects the increased damping that is given by the graphene reinforcement, which is an important outcome of this study. The comparison directly shows how the resonant response of graphene-reinforced composites is altered and dynamic stability is improved by the reduction of long-lasting, high-amplitude vibrations, which is a critical factor in the design of structures that will be exposed to dynamic loads.

Under two different loading conditions, the Fig. 5 demonstrates the transient central deflection response of the graphene-reinforced composite plate with the same normalized scale. It is most likely that the "Static" curve represents a step or constant load, and it initially shows a rapid rise to a maximum deflection, followed by a decaying oscillation. It has already reached the response of the structure's inherent damping and its transfer from dynamic to static equilibrium through the decay process. On the other hand, the "Harmonic Impact" curve indicates the response to a suddenly applied oscillatory force. It has a more sophisticated transient signature, which is marked by a strong initial peak and followed by oscillations that are maintained. These oscillations happen because of the natural vibration modes of the plate (which have been excited by the impact) and the ongoing external harmonic forcing working together. The direct comparison shows one of the key points of the study very clearly: dynamic overshoot and long-lasting vibrational activity when time-varying loads are applied are greatly more severe than the static load of similar magnitude, causing the same response. The visual demonstration strengthens the argument for the sophisticated analytical methodology of SSDT, Fourier expansion, and Laplace transform inversion to accurately predict and mitigate these dynamic effects, which is indispensable for their very existence. The rapid decay visible in both responses, however, is a clear sign that the graphene

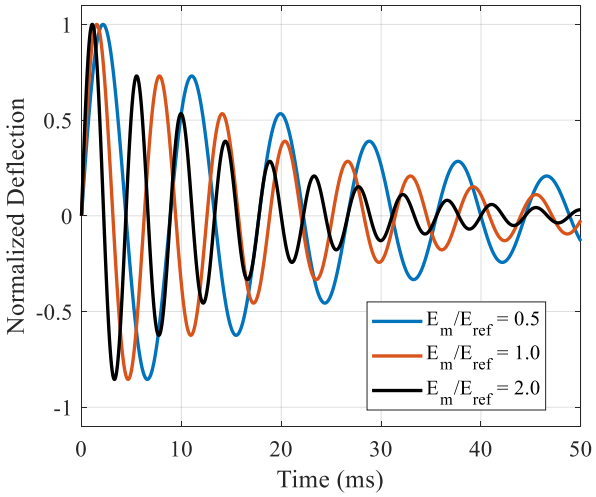

Figure 7. Transient dynamic response of the graphene-reinforced composite plate for different values of matrix material's stiffness

composite has greater damping performance, which is a factor that enhances the material's resilience under such dynamic conditions.

Fig. 6 illustrates the impact of thickness on the plate's dynamic response, which is an important consideration for structural design. The graph shows the three thickness ratios: a thinner plate, a reference plate, and a thicker plate compared by their central deflection normalized over time. Generally, thicker plates possess a higher stiffness in bending. This is seen in the case of the thickest plate with its pronounced deflection completely eliminated, therefore, only minor oscillations are seen. On the other hand, the plate with the smallest thickness has low-frequency, large amplitude vibrations, indicating that the plate is quite compliant. Furthermore, the decay of the oscillations is faster for the thicker plates, and this is indicative of the increase in the effective damping ratio. It thus implies that the damping attributed to the graphene composite is not solely determined by the material properties but it has to do with the geometry of the structure as well. The mathematical model, which is based on the SSDT, fits this interaction very well because it considers shear deformations, which are more pronounced in moderately thick plates. The result guides the designer to optimize not only the material distribution (GPL pattern) but also the geometrical parameters to ensure the desired vibration suppression in graphene-reinforced composites subjected to dynamic loads.

The matrix material's stiffness is the parameter in focus of Fig. 7, which is the transient dynamic response of the graphene-reinforced composite plate. The graph depicts the normalized central deflection over time for three ratios of the matrix Young's modulus relative to a reference value. A firmer matrix has a considerable effect on the reduction of the vibration amplitude and the speed of the oscillation's decay. On the contrary, a softer matrix causes the largest vibrations and the slowest decay, which means that the material has lower effective stiffness and damping. This pattern indicates that the whole dynamic behavior of the composite material is determined by the combined effect of the graphene reinforcement and the polymer matrix. The graphene platelets give the composite better characteristics mainly through load transfer and constraint mechanisms, the efficiency of which is, by the matrix's competence to couple with and distribute stress to the

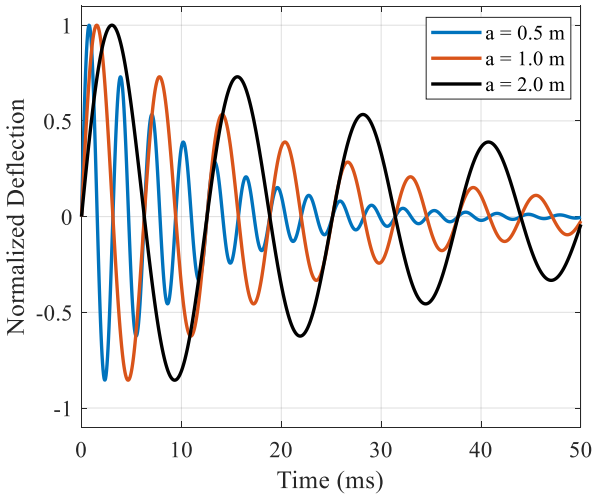

Figure 8. The effect of plate length as a parameter on the transient dynamic deflection of the graphene-reinforced composite

reinforcements, inherently modulated. Therefore, while graphene addition universally improves the performance, the absolute dynamic stability—transient deflection and decay rate measured here—still depends on the base matrix properties. This parametric knowledge is crucial for the proper design of material systems, as it confirms that the study's analytical framework can accurately depict the interaction between the individual properties and the overall dynamic behavior during external excitation.

Fig. 8 presented in this section illustrates the effect of plate length (a) as a parameter on the transient dynamic deflection of the graphene-reinforced composite. It shows a comparison of the normalized central deflection over time for three different plate lengths: a plate of 0.5 m which is shorter, a plate of 1.0 m taking as reference, and a plate of 2.0 m which is longer, while the other geometric parameters like width (b) and thickness (h) are kept constant. The results reveal a distinct pattern: the longer the plate the greater the deflection amplitudes and the slower the oscillation decay. The longest plate (a = 2.0 m) is the one that gives the most compliant response with very noticeable and lasting vibrations that come from its lower relative bending stiffness. On the other hand, the shortest plate (a = 0.5 m) is very rigid and its vibration is almost imperceptible and very quickly stopped. The parametric study thus indicates the significant interaction between the reinforcement of materials and the overall geometry. Graphene nanoplatelets, on one hand, increase the composite's specific stiffness and damping, but on the other hand, they lose their power to control transient vibrations due to the structural slenderness defined by the aspect ratio. The SSDT-based analytical model is very good at depicting this scale-dependent behavior, and this is very important for the design of large-span structural components. Thus, the figure aids in the selection of both material composition and the dimensions of the geometry which will yield the desired dynamic performance under external excitation.

Fig. 9 contrasts the graphene-reinforced composite plate's dynamic response to two basic types of temporal loadings: a continuous harmonic force and a sharp impact. The "Sinusoidal" curve illustrates the steady-state forced vibration due to the continuous harmonic excitation characterized by periodic oscillations of constant amplitude and frequency. On the contrary, the "Step Decaying"

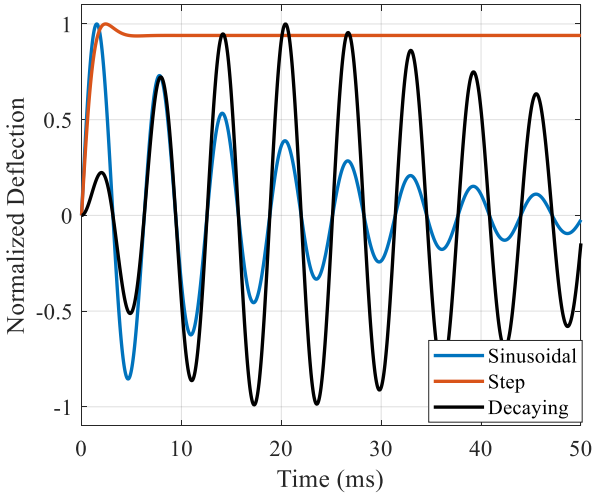

Figure 9. The graphene-reinforced composite plate's dynamic response to two basic types of temporal loadings: a continuous harmonic force and a sharp impact

curve shows the temporary response to a sudden step load, where there is a peak deflection at the start, followed by a decay of free vibrations at the system's natural frequency. The comparison reveals the analytical model's ability to deal with a variety of dynamic situations. The sinusoidal response is determined by resonance characteristics and the forcing function which is directly linked to the Fourier series solution method. The step-decaying transient, which is critical for impact analysis, is precisely resolved using the Laplace transform inversion technique mentioned in the abstract. The quick decay of the free vibrations in the step response clearly illustrates the enhanced damping due to the graphene reinforcement and thus provides a clear visual quantification. This comparative study draws attention to the structure's susceptibility to sudden impacts rather than to periodic loads and at the same time, it confirms the proposed framework as an all-encompassing tool for the prediction of both forced and transient vibrations in advanced composite plates.

Fig. 10 shows the frequency response spectrum of the composite plate with a graphene reinforcement, where dimensionless amplitude is plotted against normalized excitation frequency for three different mass ratios (0.8, 1.0, 1.2). The typical resonant peak is located around 1, where the forcing frequency is the same as the system's fundamental natural frequency. The main impact of the rising mass ratio—which probably indicates a higher mass density due to the additional graphene content—is the descending trend of the resonant peak amplitude and a small change in the peak's position. This shows two main effects of the graphene: better damping (lowering the peak) and change in the stiffness-to-mass ratio (frequency shift). The peak reduction in all mass ratios visibly confirms the improved dynamic stability and resonant vibrations suppression mentioned in the abstract. This spectrum is obtained directly from the analytical approach using Fourier expansion, measuring the degree to which graphene reinforcement can be adjusted to avoid critical resonant responses. The findings are very helpful in terms of design, as they indicate the choice of reinforcement ratios for the implementation of vibration control over a given frequency range, thus allowing one to directly associate material composition with predictable dynamic performance.

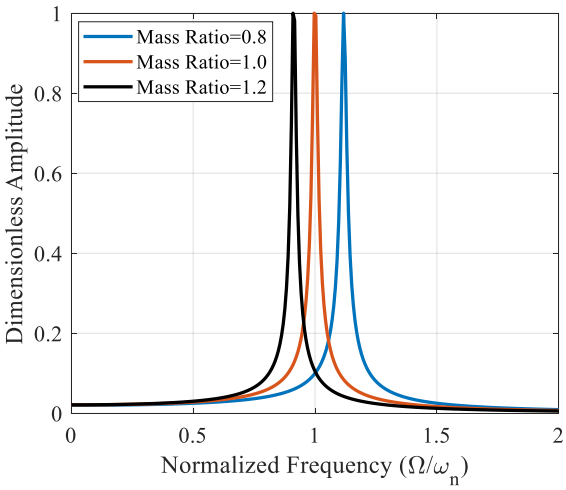

Figure 10. The frequency response spectrum of the composite plate with a graphene reinforcement, where dimensionless amplitude is plotted against normalized excitation frequency for three different mass ratios

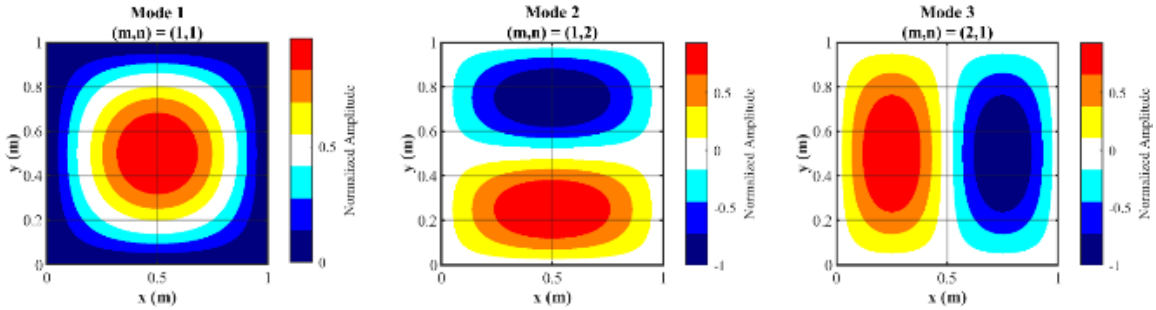

Figure 11. The modal response of the graphene-reinforced composite plate, presenting the normalized deflection curves for three different vibration mode shapes

Fig. 11 depicts the modal response of the graphene-reinforced composite plate, presenting the normalized deflection curves for three different vibration mode shapes, each indicated by a pair of mode numbers (m, n). The numbers indicate how many half-waves fit along the length of the plate (m) and width (n). Mode 1 (m,n) = (1,1) illustrates the most basic or fundamental mode, which consists of a single, centrally symmetric half-wave in both directions, therefore, a maximum deflection at the center of the plate. Mode 2 (m,n) = (1,2) resembles its predecessor, yet it has a more intricate form with one half-wave along the length and two along the width, thus, a nodal line (a line of zero displacement) is formed running parallel to the x-axis. Mode 3 (m,n) = (2,1) is the opposite of Mode 2, with two half-waves along the length and one along the width, hence, a nodal line existing parallel to the y-axis. The figure is a comparison of the temporal decay of the aforementioned modes resulting from the same initial excitation. The analytical solution that was obtained using Hamilton's principle and SSDT automatically includes these modes through the Fourier series expansion referred to in the abstract. The graph indicates that while all modes gain from the damping property of graphene, their decay rates and the amplitudes corresponding to each mode differ. This modal decomposition is indispensable as any external force applied will

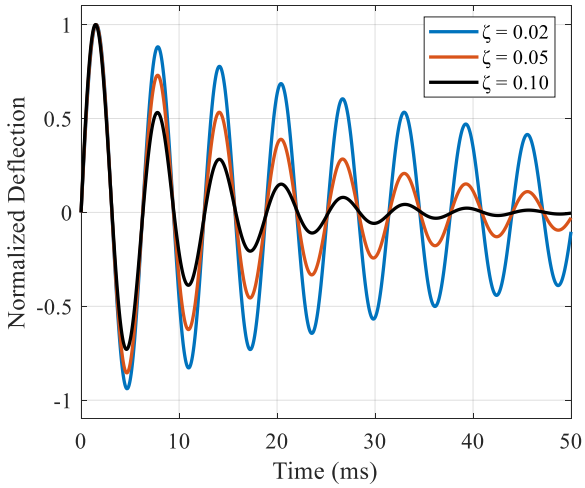

Figure 12. The abortion of damping ratio as a parameter that is influential in the graphene reinforced composite plate's dynamic transient response

result in a superposition of individual mode responses equaling the total transient response. The study endorses the model's competency to not only forecast the global response but also to reveal the extent of participation and the damping of higher-order modes, which is a prerequisite for precision in dynamic design and the avoidance of complex resonant conditions in advanced composite structures.

Fig. 12 delineates and investigates the abortion of the damping ratio (ζ) as a parameter that is influential in the graphene reinforced composite plate's dynamic transient response. It shows the normalized central deflection against time for the mentioned three damping ratios a low (ζ = 0.02), a medium (ζ = 0.05), and a high (ζ = 0.10) one. The outcomes clearly demonstrate the basic principle of viscous damping in structural dynamics. The least damped response (ζ = 0.02) is characterized by large amplitude, non-decaying oscillations, and a very slow decay. The increase in damping ratio leads to a substantial decrease in both the amplitude of the first peak and the length of the oscillatory transient. The graph for ζ = 0.10 displays rapid decay to nearly resting state in just a few cycles. This parametric research is of great importance for both validation and design processes. It assures that the further damping noticed in the graphene-reinforced composites (as indicated in previous figures) can be represented as a viscous damping ratio in the analytic framework. Apart from that, it expresses the dynamic response sensitivity to this parameter, thus providing the engineers with a direct link between the power of the material's intrinsic damping (made possible by graphene addition) and the control of transient deflection. This means that composites can be designed with the specific objective of achieving the required damping ratio that will give good performance during vibration suppression either by impact or by harmonic loads.

Fig. 13 displays the frequency response spectrum of the composite plate, showing dimensionless amplitude versus normalized excitation frequency for the three damping ratios considered. The frequencies used for the study were ζ=0.01,0.02,0.05. The frequency domain shows the steady-state level of the system forced by an external periodic input through a frequency sweep, with the input frequency pointed at the resonance. Damping is the main factor that determines the shape of

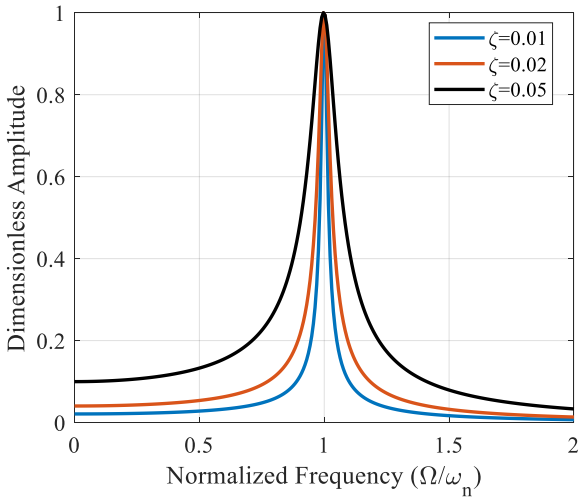

Figure 13. The frequency response spectrum of the composite plate, showing dimensionless amplitude versus normalized excitation frequency for the three damping ratios.

the curves and the vibration of the system at resonance. The lowest ratio, ζ=0.01, gives a very sharp high peak, which signifies a very narrow and deep resonant slot where energy is amplified severely. The peak of resonance is the same, but in the case when the damping ratio is raised to the level of ζ=0.05, the peak is remarkably weakened and stretched, marking a decrease in maximum amplitude and less receptiveness to frequency changes. Thus, this image quantitatively correlates the damping capability of the material being tested, made more effective with the presence of graphene, to a crucial performance parameter: the reduction of resonant amplitudes. The spectrum is achieved directly through the application of the analytical method based on the Fourier series expansion. It is an important source of design insight, indicating at the same time that increased damping (which can be obtained through the appropriate distribution of graphene) not only decreases the maximum deflections but also enhances the structural dynamic stability over the whole frequency range, thus preventing the dangers connected to the application or environmental excitations close to resonance.

6. Conclusion

The analysis of the transient dynamic behavior for external excitations of the graphene-reinforced composite plates in this research has been quite extensive, and their vibration characteristics have been uncovered. The motion equations have been formulated thanks to the application of SSDT and Hamilton's principle, which gives a reliable foundation for the considered elastic and viscoelastic behavior in composite structures. The Fourier expansion was instrumental in breaking down the dynamic response to harmonics, which has greatly advanced the comprehension of the temporary deflections of these materials. The application of Laplace transforms inversion method, particularly by Dubner and Abate's modified algorithm, has turned out to be an efficient and accurate solution of the transient dynamic problem. The results demonstrated the positive impact of graphene reinforcement on the dynamic properties of

composite plates. Graphene-reinforced composites have shown excellent damping characteristics, shifted resonance frequencies, and better stability with the external excitations. The changes have been especially prominent at different excitation frequencies, which means that graphene has the potential to be a game-changer in the field of composite structures in terms of their vibrational properties. The analytical framework for advanced graphene-reinforced composite materials has been established through this research, which is now applicable to a wide range of engineering applications. The findings will have an impact on the aerospace, automobile, and civil engineering, among others, where vibration control and material performance under dynamic loading are essential. Besides, the methods that have been developed in this study can also be applied to other composite materials and structural configurations, thus allowing future research in dynamic analysis and material optimization. In summary, this study has provided a significant amount of knowledge to the advanced material research field and has opened up new avenues for the development of high-performance composite structures.

Acknowledgment

This research is funded by Zarqa University

References

1. Allahkarami, F., Tohidi, H. (2023). Axisymmetric postbuckling of functionally graded graphene platelets reinforced composite annular plate on nonlinear elastic medium in thermal environment. International Journal of Structural Stability and Dynamics, 23, 2350034. https://doi.org/10.1142/S0219455423500347
2. Babaei, H., Zavari, S., Kaveh, A., Arshid, E., Civalek, Ö. (2025). Dynamic response of advanced lightweight porous plates integrated with nanocomposite face sheets resting on elastic substrate. International Journal of Structural Stability and Dynamics, 25, 2550132. https://doi.org/10.1142/S0219455425501329
3. Li, J., Liu, J. (2025). Nonlinear optimized PID vibration control of thermal-dependent FG composite porous plates reinforced by agglomerated CNTs. International Journal of Structural Stability and Dynamics, 25, 2550034. https://doi.org/10.1142/S0219455425500348
4. Ren, Z., Cao, L., Zhou, H., Liu, J., Li, J. (2025). Three-dimensional walking load based on bipedal variable damped spring-loaded inverted pendulum model. International Journal of Structural Stability and Dynamics. https://doi.org/10.1142/S0219455427500933
5. Rahimi, A., Alibeigloo, A., Safarpour, M. (2020). Three-dimensional static and free vibration analysis of graphene platelet–reinforced porous composite cylindrical shell. Journal of Vibration and Control, 26, 1627-1645. https://doi.org/10.1177/1077546320902340
6. Al-Houri, S., Al-Osta, M.A., Bourada, F., Gawah, Q., Tounsi, A., Al-Dulaijan, S.U. (2024). Analysis of porosity-dependent wave propagation in FG-CNTRC beams utilizing an integral higher-order shear deformation theory. International Journal of Structural Stability and Dynamics, 2550233. https://doi.org/10.1142/S0219455425502335
7. Adeniyi, A.G., Abdulkareem, S.A., Iwuozor, K.O., Abdulkareem, M.T., Adeyanju, C.A., Emenike, E.C., Ndagi, M., Akande, O.J. (2023). Mechanical and microstructural properties of expanded polyethylene powder/mica filled hybrid polystyrene composites. Mechanics of Advanced Materials and Structures, 30, 2610-2619. https://doi.org/10.1080/15376494.2022.2059822
8. Abderezak, R., Rabia, B., Daouadji, T.H., Abbes, B., Belkacem, A., Abbes, F. (2018). Elastic analysis of interfacial stresses in prestressed PFGM-RC hybrid beams. Advances in Materials Research, 7(2),

83-96. https://doi.org/10.12989/amr.2018.7.2.083
9. Tyona, M. (2013). A theoretical study on spin coating technique. Advances in Materials Research, 2(4), 195-208. https://doi.org/10.12989/amr.2013.2.4.195
10. Zhang, J., Yang, X., Zhang, W. (2018). Free vibrations and nonlinear responses for a cantilever honeycomb sandwich plate. Advances in Materials Science and Engineering, 2018, 1-12. https://doi.org/10.1155/2018/8162873
11. Rabczuk, T., Areias, P., Belytschko, T. (2007). A meshfree thin shell method for non-linear dynamic fracture. International Journal for Numerical Methods in Engineering, 72, 524-548. https://doi.org/10.1002/nme.2013
12. Rabczuk, T., Gracie, R., Song, J., Belytschko, T. (2010). Immersed particle method for fluid-structure interaction. International Journal for Numerical Methods in Engineering, 81, 48-71. https://doi.org/10.1002/nme.2670
13. Rabczuk, T., Ren, H., Zhuang, X. (2019). A nonlocal operator method for partial differential equations with application to electromagnetic waveguide problem. Computers, Materials & Continua, 59, 31-55. https://doi.org/10.32604/cmc.2019.04168
14. Eshaghi, M.S., Anitescu, C., Thombre, M., Wang, Y., Zhuang, X., Rabczuk, T. (2025). Variational physics-informed neural operator (vino) for solving partial differential equations. Computer Methods in Applied Mechanics and Engineering, 437, 117785. https://doi.org/10.1016/j.cma.2024.117785
15. Liu, B., Wang, Y., Rabczuk, T., Olofsson, T., Lu, W. (2024). Multi-scale modeling in thermal conductivity of Polyurethane incorporated with Phase Change Materials using Physics-Informed Neural Networks. Renewable Energy, 220, 119565. https://doi.org/10.1016/j.renene.2023.119565
16. Fu, T., Wang, X., Rabczuk, T. (2024). Broadband low-frequency sound insulation of stiffened sandwich PFGM doubly-curved shells with positive, negative and zero Poisson's ratio cellular cores. Aerospace Science and Technology, 147, 109049. https://doi.org/10.1016/j.ast.2024.109049
17. Guo, H., Zhuang, X., Fu, X., Zhu, Y., Rabczuk, T. (2023). Physics-informed deep learning for three-dimensional transient heat transfer analysis of functionally graded materials. Computational Mechanics, 72, 1-12. https://doi.org/10.1007/s00466-023-02378-9
18. Safarpour, H., Safarpour, M., Jamali, J., Civalek, Ö. (2025). Sound radiation and phase velocity characteristics of FG bio-composite annular plates. Journal of Vibration Engineering & Technologies, 13, 366. https://doi.org/10.1007/s42417-025-01936-0
19. Guo, P., Zhang, Y., Xi, Y., Saleem, K., El-Meligy, M., Safarpour, H. (2024). Nonlinear transient deflections of multi-layer sector plate structures on auxetic concrete foundation: introducing an artificial intelligence algorithm for nonlinear problems. Structures, 70, 107563. https://doi.org/10.1016/j.istruc.2024.107563
20. Safarpour, M., Forooghi, A., Dimitri, R., Tornabene, F. (2021). Theoretical and numerical solution for the bending and frequency response of graphene reinforced nanocomposite rectangular plates. Applied Sciences, 11, 6331. https://doi.org/10.3390/app11146331
21. He, X., Ding, J., Habibi, M., Safarpour, H., Safarpour, M. (2021). Non-polynomial framework for bending responses of the multi-scale hybrid laminated nanocomposite reinforced circular/annular plate. Thin-Walled Structures, 166, 108019. https://doi.org/10.1016/j.tws.2021.108019
22. Rashvand, K., Alibeigloo, A., Safarpour, M. (2022). Free vibration and instability analysis of a viscoelastic micro-shell conveying viscous fluid based on modified couple stress theory in thermal environment. Mechanics Based Design of Structures and Machines, 50, 1198-1236. https://doi.org/10.1080/15397734.2020.1744005
23. Guo, H., Zhuang, X., Rabczuk, T. (2021). A deep collocation method for the bending analysis of Kirchhoff plate. arXiv Preprint, arXiv:2102.02617.
24. Zhuang, X., Guo, H., Alajlan, N., Zhu, H., Rabczuk, T. (2021). Deep autoencoder based energy method for the bending, vibration, and buckling analysis of Kirchhoff plates with transfer learning. European Journal of Mechanics-A/Solids, 87, 104225. https://doi.org/10.1016/j.euromechsol.2021.104225
25. Samaniego, E., Anitescu, C., Goswami, S., Nguyen-Thanh, V.M., Guo, H., Hamdia, K., Zhuang, X., Rabczuk, T. (2020). An energy approach to the solution of partial differential equations in

computational mechanics via machine learning: concepts, implementation and applications. Computer Methods in Applied Mechanics and Engineering, 362, 112790. https://doi.org/10.1016/j.cma.2020.112790

26. Safarpour, M., Rahimi, A., Alibeigloo, A., Bisheh, H., Forooghi, A. (2019). Parametric study of three-dimensional bending and frequency of FG-GPLRC porous circular and annular plates on different boundary conditions. Mechanics Based Design of Structures and Machines, 47, 1-31. https://doi.org/10.1080/15397734.2019.1662310
27. Wang, Y., Zeng, R., Safarpour, M. (2020). Vibration analysis of FG-GPLRC annular plate in a thermal environment. Mechanics Based Design of Structures and Machines, 48, 1-19. https://doi.org/10.1080/15397734.2020.1719508
28. Rahimi, A., Alibeigloo, A. (2020). High-accuracy approach for thermomechanical vibration analysis of FG-GPLRC fluid-conveying viscoelastic thick cylindrical shell. International Journal of Applied Mechanics, 12, 2050073. https://doi.org/10.1142/S1758825120500738
29. Safarpour, M., Rahimi, A.R., Alibeigloo, A. (2020). Static and free vibration analysis of graphene platelets reinforced composite truncated conical shell, cylindrical shell, and annular plate using theory of elasticity and DQM. Mechanics Based Design of Structures and Machines, 48, 496-524. https://doi.org/10.1080/15397734.2019.1646137
30. Reddy, J.N. (2003). Mechanics of laminated composite plates and shells: theory and analysis. CRC Press, Boca Raton, FL, USA.
31. Nguyen, S.N., Cho, M., Kim, J.S., Han, J.W. (2022). Improved thermo-mechanical-viscoelastic analysis of laminated composite structures via the enhanced Lo-Christensen-Wu theory in the Laplace domain. Mechanics of Advanced Materials and Structures, 30, 1-17. https://doi.org/10.1080/15376494.2022.2097206
32. Durbin, F. (1974). Numerical inversion of Laplace transforms: an efficient improvement to Dubner and Abate's method. The Computer Journal, 17, 371-376. https://doi.org/10.1093/comjnl/17.4.371
33. Lee, Y., Zhao, X., Liew, K.M. (2009). Thermoelastic analysis of functionally graded plates using the element-free kp-Ritz method. Smart Materials and Structures, 18, 035007. https://doi.org/10.1088/0964-1726/18/3/035007
34. Nguyen-Xuan, H., Tran, L.V., Nguyen-Thoi, T., Vu-Do, H. (2011). Analysis of functionally graded plates using an edge-based smoothed finite element method. Composite Structures, 93, 3019-3039. https://doi.org/10.1016/j.compstruct.2011.04.028
35. Gilhooley, D., Batra, R., Xiao, J., McCarthy, M., Gillespie Jr, J. (2007). Analysis of thick functionally graded plates by using higher-order shear and normal deformable plate theory and MLPG method with radial basis functions. Composite Structures, 80, 539-552. https://doi.org/10.1016/j.compstruct.2006.07.007